JOURNAL OF AIRCRAFT
Vol. 43, No. 6, November–December 2006

Evaluation of a Three-Degree-of-Freedom Test Rig for Stability Derivative Estimation

A. Gatto* and M. H. Lowenberg†
University of Bristol, Bristol, BS8 1TR England, United Kingdom

DOI: 10.2514/1.19821

This paper details a quantitative investigation into a cost-effective, three degree-of-freedom test rig to determine aircraft static and dynamic stability derivatives. The technique used a specifically designed three degree-of-freedom gimbaled mechanism to connect an actively controlled model to a vertical support strut. The support strut was also mounted on a six-component piezoelectric balance to obtain aerodynamic force and moment data simultaneously with the model motion. With only minor modifications to the overall setup, a comprehensive set of static and dynamic stability derivatives were obtained which showed reasonable to good agreement with other, independently obtained, data.

Nomenclature

b	=	wing span
C_X	=	horizontal force coefficient in wind axes, $-C_D$
C_Y	=	side force coefficient in wind axes
C_Z	=	vertical force coefficient in wind axes, $-C_L$
C_1	=	roll moment coefficient
C_m	=	pitching moment coefficient
C_n	=	yawing moment coefficient
$\bar{\bar{c}}$	=	mean aerodynamic chord
g	=	acceleration due to gravity
I	=	moment of inertia
I_{xx}	=	moment of inertia in roll
I_{yy}	=	moment of inertia in pitch
I_{zz}	=	moment of inertia in yaw
K_n	=	static margin
k	=	reduced frequency, $\omega\bar{\bar{c}}/2V_o$, $\omega b/2V_o$, induced drag factor
L	=	length of trifilar support wires
M	=	mass of model
p, q, r	=	angular rates
R	=	radius of trifilar base to support wires
t, T	=	time
u, v, w	=	velocity components
V_o	=	freestream velocity
α	=	angle of attack
β	=	angle of sideslip, $-\psi$
ϕ, ψ	=	roll and yaw angles
η	=	stabilator angle
ξ	=	aileron angle
ζ	=	rudder angle, damping
δ	=	increment
ω	=	circular frequency

I. Introduction

EVEN with the rapid advances in computational fluid dynamics methods for the prediction of aircraft stability derivatives, the search for new and improved experimental testing techniques continues unabated. The primary impetus for this effort remains the inability of predictive methods to adequately quantify stability derivatives, particularly dynamic, in regimes where high angles of attack and nonlinear dynamics dominate [1,2]. To tackle this problem, many experimental techniques have been developed over the years to estimate both static and dynamic stability parameters with most able to provide relatively accurate and reliable estimates of the derivatives sought. However, these techniques are often optimized to obtain data in a specific test regime with many only able to obtain a few of the complete set of derivatives desired. This situation, unfortunately, has compelled the designer to use multiple techniques to obtain the critical design data required, resulting in the costly and labor intensive test programs that are common practice today.

Predominantly, most testing techniques suffer from a combination of high complexity [2–9], excessive setup and/or running costs [3,10], intrusive and interference effects [4,11], limited motion capabilities [12–18], and/or the use of active feedback control [6,19,20] when pure unassisted response motion would be ideal. Perhaps the most inhibitive of all of these limitations is cost. With typical expenditures for most of these systems being of the order of tens to hundreds of thousands of dollars to acquire, set up, and run, it is clear that a major barrier exists to all but the largest of corporations for investing in a comprehensive and robust test program. A single system, which is cost-effective, efficient, and capable of obtaining the majority of stability data required, particularly for the quick evaluation at early design stages, remains illusive.

In an attempt to fulfill this goal, this work presents a technique that merges the capabilities of many of the currently used techniques just described. A specifically designed, three degree-of-freedom gimbal, ventrally installed in the test model, is used in conjunction with an actively controlled model. Additionally, the gimbal is mounted on a vertical support strut which is fixed to the wind tunnel floor via a six-component force and moment balance. The two main components of the system, the balance and the model, can be of the order of thousands of dollars to acquire and set up in this manner, representing a significant reduction in initially incurred costs over other methods.

II. Experimental Setup and Procedure

A. The M2370 Flight Vehicle

A general layout of the QinetiQ, Ltd., designated, full scale, M2370 configuration 1 model, used for all testing is shown in Fig. 1. The model was constructed of carbon fiber and had a diamond wing planform together with leading edge strakes running along the leading portion of the central fuselage. Facilitated in the design of the model was a 30 mm adjustment in the distance between the center of gravity and the aerodynamic center of the model. This allowed the

Received 1 September 2005; revision received 24 March 2006; accepted for publication 26 March 2006.

*Research Associate, Department of Aerospace Engineering, University of Bristol, Bristol, BS8 1TR England, United Kingdom.

†Senior Lecturer, Department of Aerospace Engineering, University of Bristol, Bristol, BS8 1TR England, United Kingdom. Senior Member AIAA.

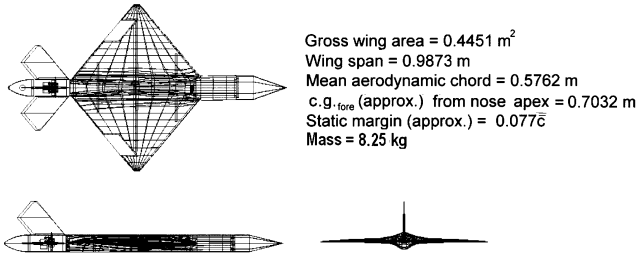

Fig. 1 The M2370 flight vehicle.

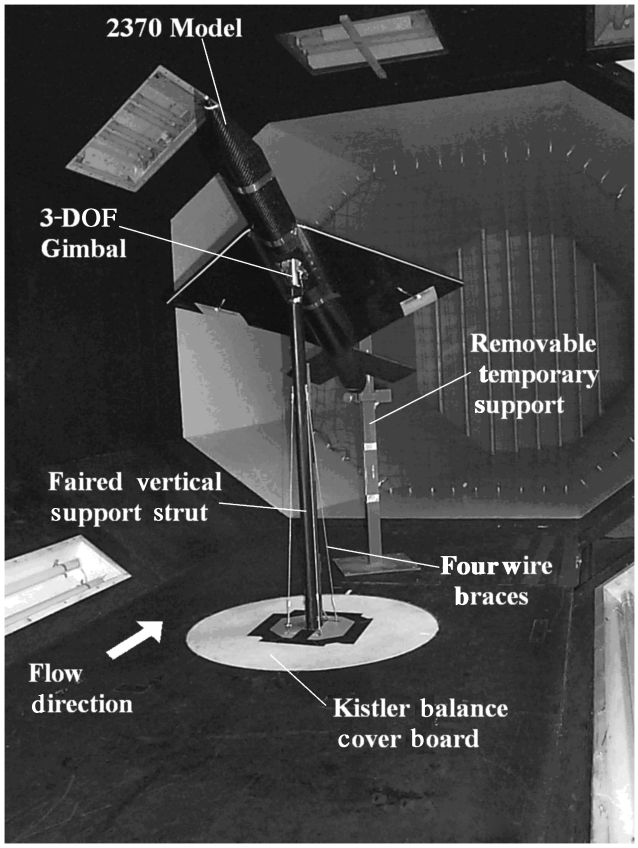

Fig. 2 The wind tunnel setup for dynamic testing.

static margin of the model to be adjusted and was achieved through the movement of an internally mounted cavity tray.

B. Instrumentation and Hardware

The M2370 flight vehicle used all-moving stabilators, ailerons, and rudder. Maximum limits of deflection for these three control surfaces were found to be better than ±30, ±20, and ±30 deg, respectively. Digital servos were used to actuate all of the control surfaces via a dedicated driver board and a DIMMPC running purpose built software. Measurement of each control surface angular position was obtained by directly coupled, precision potentiometers, connected to a Diamond MM-33-AP data acquisition board sampling at 50 Hz. After each run, all measured data were automatically stored to a flash memory card located in the tail of the model for later analysis. A calibration of the control surface position before "wind on" conditions, and under no load, was found to produce a control surface position uncertainty of less than ±2.5 deg.

The wind tunnel used for all tests was a 9×7 ft, closed test section, closed circuit wind tunnel, owned by BMT Fluid Mechanics, Ltd., in Teddington, London. The maximum freestream velocity achievable in the test section was 60 m/s, with the test speed selected for this investigation set at 26 m/s. This gave a test Reynolds number of 1.02×10^6. The feedback control system used to control tunnel speed in the test section was rated at ±0.5 m/s, with the turbulence intensity, measured at the model station, found to be approximately 0.25%. No blockage or support interference effects, excluding support tare corrections, were taken into account for this investigation.

The apparatus used to acquire all forces and moments was a Kistler six-component piezoelectric balance. The balance uses four, type 9251 A, three component force transducers and a summing amplifier to obtain the three forces and three moments. To allow sideslip data to be obtained, the balance also had the ability to rotate 360 ± 0.1 deg from the wind tunnel centerline. Taking into account setup and model orientation error, as well as free play in the gimbal mounting system, the maximum uncertainty in the estimation of the angle of sideslip was estimated to be no more than ±1 deg. Additionally, before the initiation of the model test program, a check of the Kistler balance calibration was performed. The maximum deviation found from repeated results was less than ±2.5% for any measured component. Estimation of the maximum errors in the measurement of the nondimensional forces and yawing moment derivative were, therefore, estimated at ±0.025. Estimates of the error for the rolling and pitching moment derivatives were found to be somewhat larger at ±0.05, because of the need to use the drag and side force data to reduce these results. A more detailed description of the balance can be found in [21].

Control of the M2370 flight vehicle, together with acquiring data from the three degree-of-freedom (DOF) gimbal and the Kistler balance, were managed, in real time, by a dSpace data acquisition system. All data acquired from the setup was sampled at 1000 Hz to 16-bit precision over periods ranging, depending on the test configuration, from 20–60 seconds. Control of the flight vehicle was achieved through a linked RS232 asynchronous port situated on the controller board of the dSpace hardware and connected, via an umbilical, to a DIMMPC located inside the model. Figure 2 shows the model setup in the wind tunnel.

C. Moment of Inertia Calculation

The moment of inertia of the model about its body axes was determined using the trifilar suspension technique. This method employs a circular disc suspended from a rigid support by three equally spaced wires located around the circumference of the disc. The body, whose moment of inertia (MOI) is to be measured, is then placed on the disc in various orientations to obtain the MOI for each axis. The disc is then excited by a small amplitude excitation about the axis of rotation and the resultant simple harmonic motion is timed over several cycles. The average time for one cycle is then recorded and used in Eq. (1) to estimate the MOI.

To obtain the MOI for the M2370 model, tests were performed about each body axis of rotation for the combination of model and base. Using the same technique to find the inertia of the base alone, the MOI of the model was then estimated from subtracting the base alone result from the combined value. To assess the repeatability of the results, each test was repeated three times. Accurate location of the model c.g. during the calculation of the moment of inertia was facilitated via accurate line markers placed on, as well as specifically designed cutouts prefabricated in, the trifilar base. Estimates of the probable error in c.g. offset from the rotation axis were found to be no more than 5 mm in any direction. Contributions to the measurement of moment of inertia, from this position error, were estimated at less than 0.5%. Table 1 summarizes the results obtained.

$$I = \frac{MgR^2T^2}{4\pi L} \tag{1}$$

Table 1 Moment of inertia for the M2370 flight vehicle

	I, kgm^2	Error(95% conf.) kgm^2
Ixx	0.118	±0.039
Iyy	1.653	±0.053
Izz	1.710	±0.051

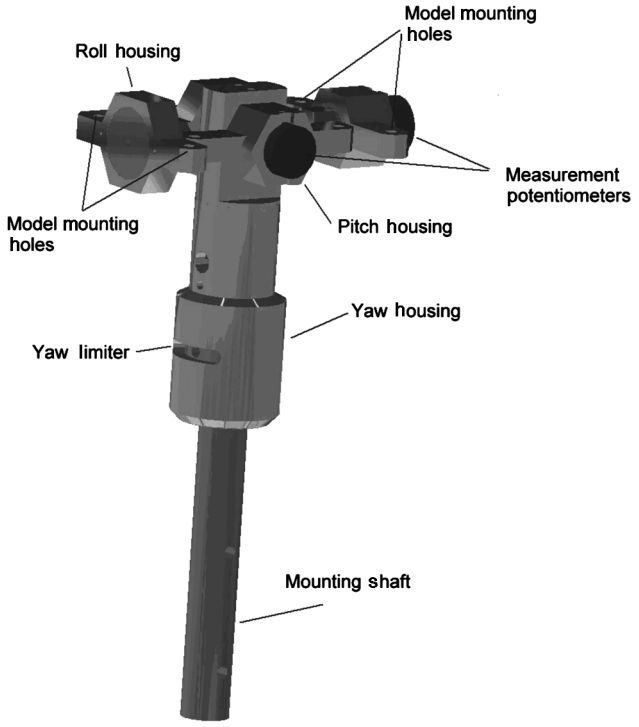

Fig. 3 3-DOF gimbal.

D. Static and Dynamic Configurations

1. Static Testing Configuration

For the static testing configuration, a DC shunt motor directly connected to a vertical leadscrew arrangement located directly behind the faired main strut was used to adjust the model pitch angle. This was achieved via an additional pitch arm (not shown in Fig. 2) connecting brackets on the leadscrew and the model tail cone. The achievable pitch range, with the M2370 flight vehicle installed, was -15 to $+25$ deg inclusive. To ensure both roll and yaw degrees of freedom were rigid during the static testing phase, a purposely designed pitch plate was installed on top of the gimbal, preventing roll, together with a yaw limiter (shown in Fig. 3), locked at $\psi = 0$ deg. To calibrate the static pitch angle, a digital inclinometer (error $= \pm 0.1$ deg) was placed on the model fuselage and measured against the reading from the pitch axis potentiometer via the dSpace interface. The uncertainty in angular position, after calibration, was estimated to be no more than ± 1 deg. This degree of accuracy was typical of the setup, with the calibration of additional measurement potentiometers for the roll and yaw axes also found to reside within this error band.

2. Dynamic Testing Configuration

For the dynamic testing configuration, the pitch arm and pitch plate were removed from the setup, and the yaw limiter released to allow free motion in pitch, roll, and yaw. For all of the dynamic testing configurations, the Kistler balance was again used to measure the dynamic lift, drag, and side force simultaneously with the model motion.

A detailed schematic of the 3-DOF gimbal is shown in Fig. 3. The design of the gimbal incorporated two housing frames, one located inside the other, and pivoted by precision ball bearings which provided free motion in pitch and roll. A third yaw housing, fixed to the inner pitch housing, utilized thrust bearings to resist the aerodynamic forces and moments generated, while providing the ability for free motion in yaw. In each of the three axes, Penny and Giles precision potentiometers were used to measure the pitch, roll, and yaw motions of the model (pitch and roll gimbals indicated in Fig. 3). The yaw potentiometer (not shown), was located inside the yaw housing and was directly coupled to the mounting shaft.

When operating with 3-DOF capability, the limits of the gimbal in pitch, roll, and yaw were ± 45, ± 45, and ± 35 deg, respectively. To reduce the impact loads on the gimbal bearings if the gimbal limit was reached, semirigid padding was placed around a cutout in the fuselage of the model. Because of the degree of angular rotation achieved from using the 3-DOF gimbal, the cutout required in the model fuselage was quite large (Fig. 2), and conceivably, would have introduced a cavity effect on the results obtained. However, no attempt has been made here to account for this effect. Additionally, to determine the stability derivatives, all angular rates and accelerations needed for the equations of motion were obtained from numerical differentiation of the angular position [16].

The model c.g. location in both the longitudinal and lateral directions, before undertaking the dynamic test program, was adjusted by placing ballast at positions around the 3-DOF gimbal mounting position until static balance over the pivot position was achieved. For all testing, the longitudinal c.g. location was positioned at approximately 0.7 m from the tip of the model nose. To provide enhanced stability in roll, the vertical location of the c.g. was fixed at approximately 5 mm below the pivot position of the gimbal. This position for the vertical c.g. was chosen due to sensitivity of the model in roll if the pivot position of the gimbal and the vertical c.g.. of the model coincided. Having the vertical c.g. located slightly below the pivot position, it was found that the ability of the model to both remain at a commanded roll orientation and return to the initial roll attitude after excitation was significantly enhanced. Ultimately, the final degree of vertical c.g. offset was also chosen as a trade-off between the model possessing sufficient static roll stability, while minimizing the impact of gravitational and inertial effects on the motion and force data.

Determination of the vertical c.g. location was performed by a trial and error process. This involved incrementing the distance between the 3-DOF gimbal mounting frame and the M2370 model chassis through the successive addition of 1 mm washers, and measuring the response of the model thereafter, to a "wind off", operator-initiated impulse excitation in roll. If the vertical c.g. location was above the level of the pivot position under impulse excitation, the model rolled to that side and would hold position. If the vertical c.g. was below the pivot position under excitation, the model would return slowly to the

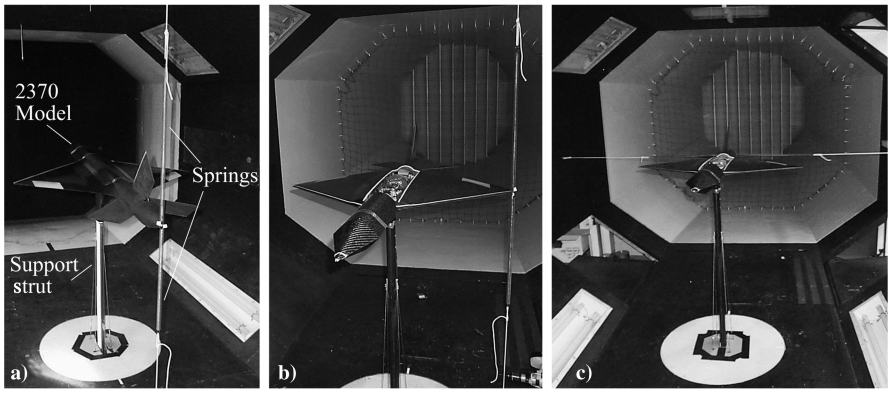

Fig. 4 Setup for determination of wind off damping: a) pitch, b) roll, and c) yaw.

Table 2 Summary of "wind off" damping characteristics for the 3-DOF gimbal/model combination

	ω_n, rads^{-1}	ζ
Pitch	4.39 ± 0.01	0.0063 ± 0.0006
Roll	8.92 ± 0.02	0.0145 ± 0.0005
Yaw	4.32 ± 0.01	0.0039 ± 0.0002

initial position though the effect of the gravity vector. The range of movement between these two extremities, taking into account the static friction of the gimbal, was found to be ± 3 mm.

To subtract the inherent friction damping of the gimbals from the model aerodynamic damping, experiments were also conducted to determine the wind off damping of the gimbal before wind tunnel testing. To obtain this information, the model was set up using a set of springs, of known stiffness constant, in the three configurations shown in Fig. 4. Exciting each degree of freedom separately, and using the locking systems described earlier, the resultant motion was recorded via the 3-DOF gimbal measurement potentiometers and the dSpace interface. Estimates of the friction damping were then reduced from curve fitting an exponentially-decaying sine waveform to the data. This procedure was repeated several times for all three model degrees of freedom with the results showing that the gimbal contributes a negligible amount to the overall damping of the system. A correction for the contribution of the gimbal damping on the results was, therefore, not applied. Table 2 summarizes the damping and natural frequencies obtained in pitch, roll, and yaw.

Under initial wind on conditions before the initiation of all excitation inputs, the model was trimmed in all three axes to a stable flying condition. This was achieved through a manual adjustment facility (resolution of 0.1 deg) configured into the dSpace control system driving the control surfaces. After the majority of excitation conditions tested, the model was found to return to its initial condition after the model response to input excitation dissipated. As expected, during excitation of each control surface, a degree of coupling between the six degrees of freedom was measured. This coupled motion was often very subtle, particularly in roll and yaw when pitch excitation was applied. The ability of this technique to measure these motions would, it seems, make it ideally suited for the estimation of cross-derivative information as well. However, as this work is an initial investigation to validate the technique, no attempt is made here to determine these derivatives.

For all results presented, the model was excited through the use of the control surfaces solely. Two primary inputs were used, a transient impulse and continuous sine wave forced oscillation. Additionally, all input excitation was performed, predominantly, about an initial model orientation at, or near, an angle of attack of zero. Under these conditions, excitation amplitudes of the control surfaces for the sine wave forced oscillation cases varied to 10 deg at frequencies ranging from 0.2–1.5 Hz. This gave a reduced frequency range k of 0.014–0.179. For the transient excitation cases, control surface amplitudes of up to ± 15 deg, at 0.2 s duration, were used.

III. Results and Discussion

A. Evaluation of Static Stability

This section presents the results from the static testing program of the M2370 flight vehicle. Among the results presented are the effects of sideslip and angle of attack on all forces and moments, as well as the control effectiveness for all three control surfaces. As will be discussed in following sections, achieving demanded control surface position under maximum aerodynamic load, particularly for the rudder, proved difficult. Therefore, control surfaces not in use during the static testing program were artificially locked in the zero deflection position. A summary of the static stability derivatives obtained together with estimates of the static margin obtained at various fixed stabilator deflection angles, are presented in Tables A1 and A2. Sine wave forced oscillation data provided by QinetiQ using an inexorable drive rig [22–24], and obtained from an identical model configuration at the same scale and Reynolds number, is included for comparison. The oscillation amplitude and frequency used for these reference results was 2 deg and 2 Hz, respectively.

1. *Influence of Sideslip*

Figure 5 shows the nondimensional force and moment data obtained from changing the degree of sideslip from -10 to 10 deg. Results for the negative range of angle of attack are included in both plots of lift and pitching moment coefficients to aid interpretation of the trend. Considering initially C_L and C_D, relatively little variation is seen with change in sideslip, both reaching a maximum at $\alpha = 25$ deg with values of $C_L = 1.22$ and $C_D = 0.55$, respectively. From the remaining plots, all show some variation with sideslip. For positive sideslip, the general trend in side force and roll moment is to decrease, even though for both of these sets of data, there is a significant degree of scatter. Additionally, these results, together with results presented for yaw moment coefficient, also show a degree of asymmetry at large angles of attack. This behavior is not uncommon

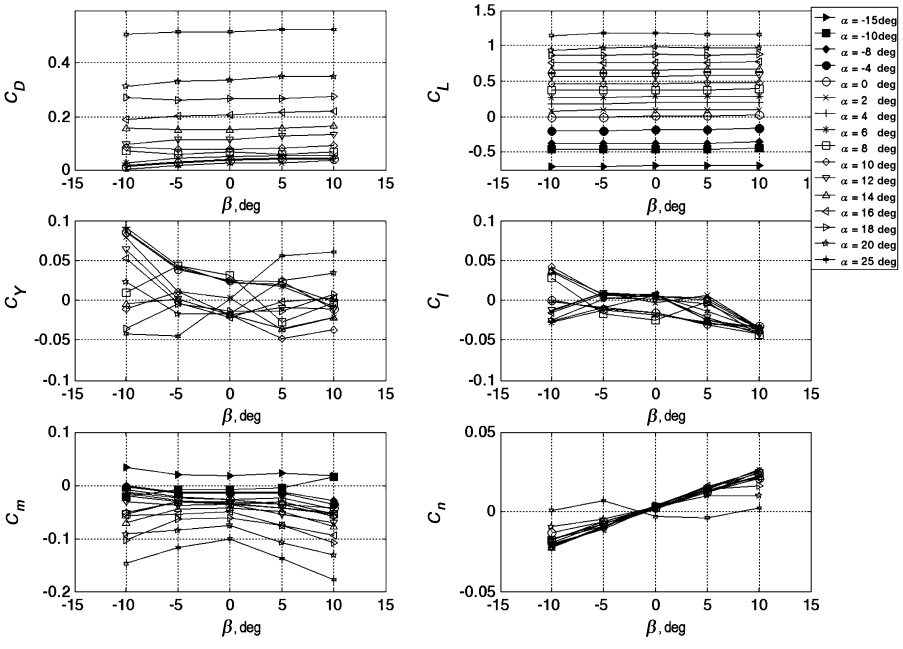

Fig. 5 Influence of sideslip on static data.

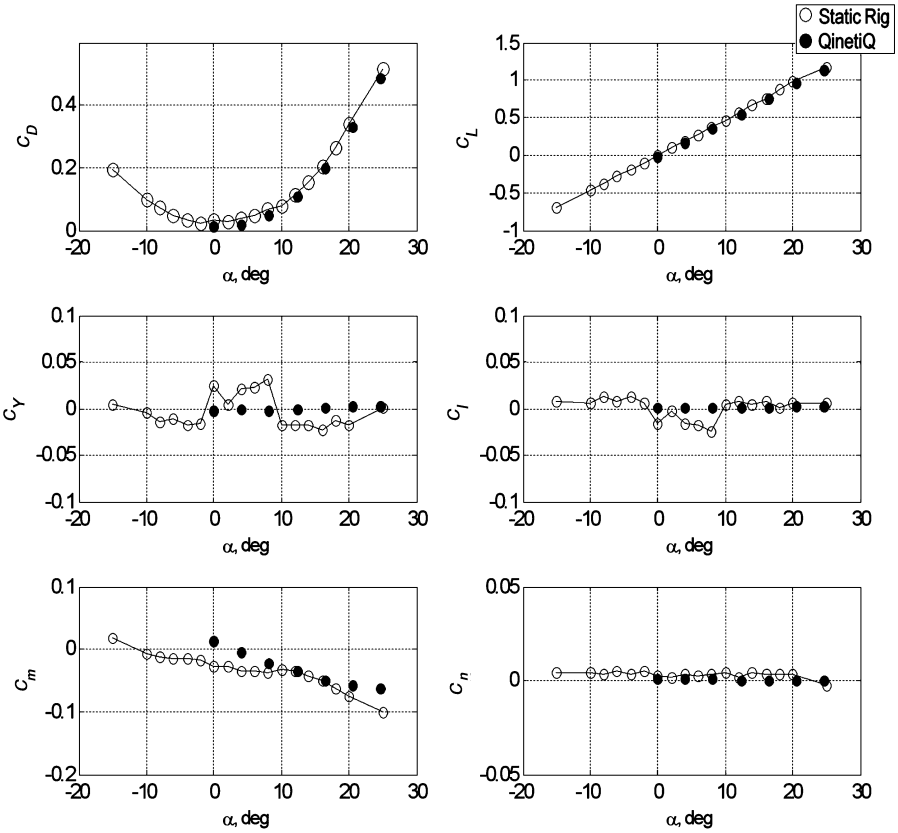

Fig. 6 Influence of angle of attack on static data.

for this type of model planform and has been shown to originate from asymmetric model aerodynamics [25–27].

Unlike the results presented for the side force and rolling moment coefficients, pitching moment coefficient shows a much more clearly definable trend with both model angle of attack and angle of sideslip. The variation of pitching moment coefficient with angle of attack shows a $\partial C_m/\partial\alpha < 0$ for all angles of sideslip indicating that, under these conditions, the model is statically stable. These results also indicate that at the extremities of sideslip and at high angles of attack, significantly larger restoring moments over those obtained for the zero sideslip condition are evident. This difference was found to be as much as 50% more, suggesting that, under zero sideslip conditions, support interference may be inhibiting stabilator effectiveness.

2. *Influence of Angle of Attack*

Figures 6 and 7 show the influence of changing the angle of attack of the model on the mean and rms force and moment coefficients at

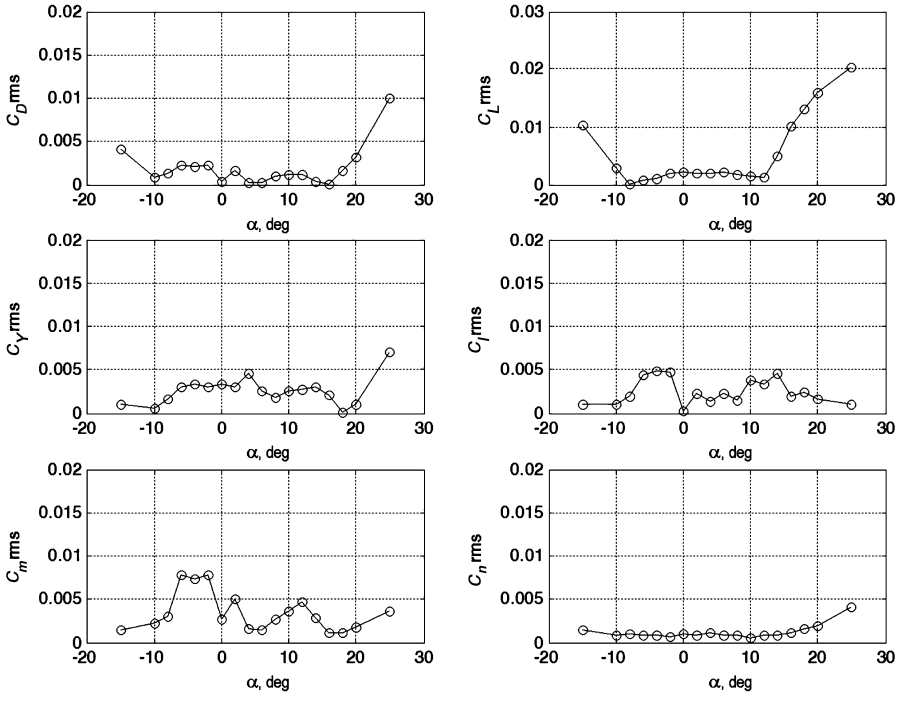

Fig. 7 Variation of rms coefficients with angle of attack.

zero sideslip. From analysis of the plots of lift and drag coefficients, the values obtained for the minimum drag coefficient and the lift curve slope were $C_{\mathrm{Do}} = 0.0227$ and $C_{L\alpha} = 2.72\,\mathrm{rad}^{-1}$, respectively. It is clear from the plot of lift coefficient that no evidence of model stall exists up to the maximum angle of attack tested. Results for both the side force and rolling moment coefficients show an unusual and discrete change in sign in the region of $0\,\mathrm{deg} \leq \alpha \leq 8\,\mathrm{deg}$. This result is unexpected and may be due to small asymmetries in the setup and/or model manufacture [25,27], as well as aerodynamic interference from the vertical support [26]. The dependency of accurate rolling moment results on the accurate determination of side force results is also clearly evident, with the disturbance clearly visible in both results.

Additional information can be drawn from considering the unsteady rms force and moment coefficients presented in Fig. 7. The most striking feature of these results is the significant increase in the degree of unsteadiness at $\alpha > 12$ and $\alpha < -8$ deg for lift coefficient, $\alpha > 16$ and $\alpha < -10$ deg for drag coefficient, and $\alpha > 20$ deg for side force coefficient. This is a clear indication of increased flow unsteadiness over the model inherent to this type of planform at these extremes [28]. Conversely, the majority of rms moment coefficients show very little definable trend. The exception to this was the yawing moment coefficient, which does indicate a significant increase in the degree of unsteadiness at $\alpha = 25$ deg, over than that shown for $\alpha < 16$ deg.

3. *Control Surface Effectiveness*

The effective stabilator power is shown in Fig. 8. All data shown are referenced to forces and moments obtained at zero stabilator deflection. From the results presented, the change in lift and pitching moment coefficients show a defined, linear trend, with change in stabilator deflection, with gradients of $C_{L\eta} = 0.492\,\mathrm{rad}^{-1}$ and $C_{m\eta} = -0.454\,\mathrm{rad}^{-1}$, respectively. As expected, all other results excluding drag coefficient show relatively weak trends. For this parameter, the variation becomes much more significant at the higher angles of attack tested, with an increase of the order of half C_{Do} at $\alpha = 8$ and $\alpha = -8$ deg, for $\eta \approx 10$ and $\eta \approx -10$ deg, respectively. Lower changes in drag coefficient are shown for positive angles of attack and negative stabilator deflections, and vice versa, due to the reduction in effective stabilator angle of attack from the freestream velocity vector. Additionally, and as expected, the change in drag coefficient is also symmetric about $\eta = 0$ deg.

Another interesting aspect of the results presented in Fig. 8 is the difference found between the demanded (η_{dem}) and actual (η_{act}) position of the stabilators under aerodynamic load. From analysis of the data points on any of the aforementioned plots, it can be seen that demanded stabilator deflection angle, with demanded inputs of $\eta = -10$ to $\eta = 10$ deg, in steps of 5 deg, were rarely achieved under test conditions. Fortunately, this was not particularly inhibitive as the actual control surface position was being measured directly via coupled potentiometers. However, it is clear that without this ability, serious implications may exist for the accuracy of results obtained using this technique.

After conducting some initial investigations, this discrepancy was found to be due to insufficient stiffness of the mounting structure supporting the control surface, and not insufficient servomotor performance as initially suspected. From a final analysis, it was determined that, at best, only approximately 90% of the demanded input was achieved at small stabilator deflections ($\eta_{\mathrm{dem}} = \pm 5$ deg) with this result degrading to approximately 70%–80% at $\eta_{\mathrm{dem}} = \pm 10$ deg. A postprocessing of these results, together with those for the ailerons and rudder, are presented in Table A3.

Aileron effectiveness is presented in Fig. 9. As would be expected, the effect of aileron deflection is shown to have a pronounced effect on both rolling and yawing moment coefficients. Analysis of the control derivatives for these two moments, at a zero angle of attack, yielded values of $C_{l\xi} = -0.068\,\mathrm{rad}^{-1}$ and $C_{n\xi} = 0.0043\,\mathrm{rad}^{-1}$, respectively. Under these conditions, therefore, adverse yaw due to aileron deflection is, in actuality, of only minor significance. At higher angles of attack, however, adverse yaw due to aileron deflection clearly increases, showing a proportionate increase at both positive and negative angles of attack. Analysis of the change in drag coefficient and change in side force results with aileron deflection also uncovers subtle variations. For the change in drag coefficient, significant aileron deflection produces a detectable increase. This result would be expected since any deflection of any control surface into the mainstream would produce a further contribution to the overall drag of the model. For the side force coefficient, the small deviations found were thought to be due to a combination of both the positioning of the ailerons (inclined to the model fuselage from Fig. 1), and that equal and opposite aileron deflection produces a net side force imbalance on the model.

Figures 10 and 11 show the results obtained from the analysis of rudder effectiveness. Additional results in this section are presented in Fig. 11 at $\beta = 10$ deg to provide an indication of the inability of the rudder to deflect to the demanded position under the highest

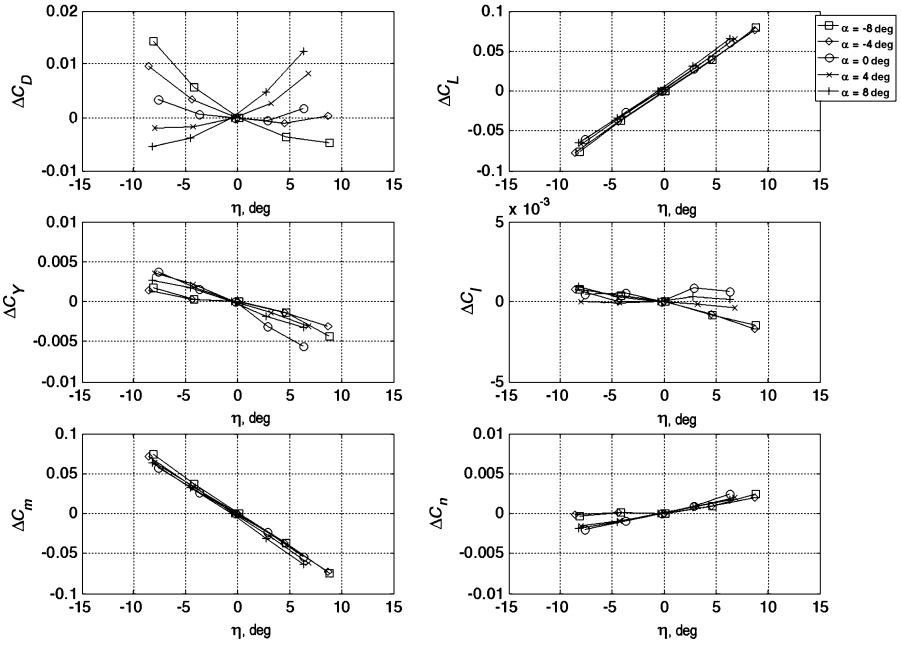

Fig. 8 Stabilator effectiveness as a function of stabilator deflection.

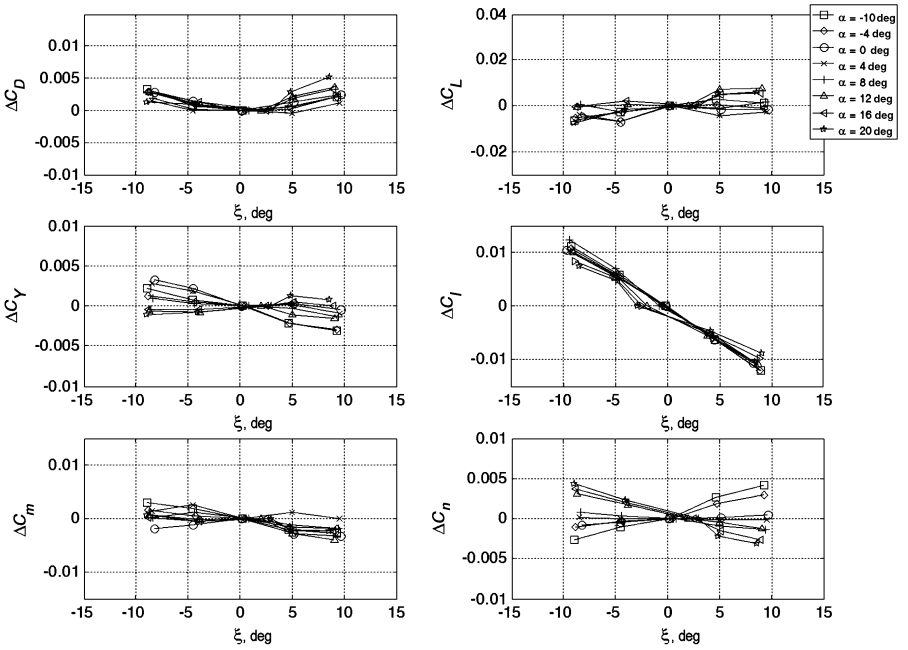

Fig. 9 Aileron effectiveness as a function of aileron deflection.

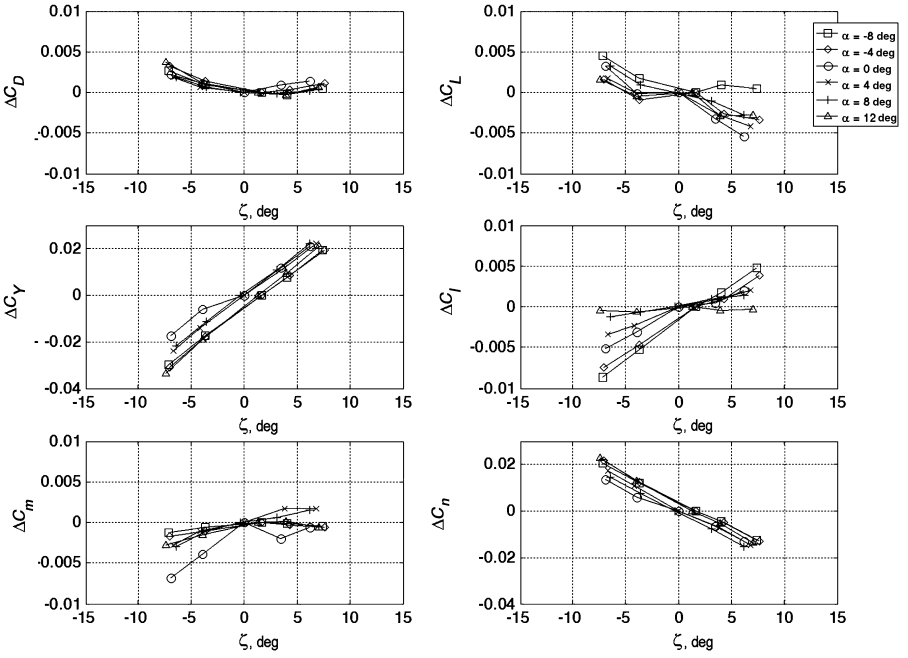

Fig. 10 Rudder effectiveness as a function of rudder deflection, $\beta = 0$ deg.

aerodynamic loading condition tested. Initially, however, from Fig. 10, the results obtained for the change in rolling, yawing, and side force coefficients, at zero sideslip, all show a significant response to rudder deflection. From analysis of these three plots, the gradients of the curves, at zero angle of attack, produced $C_{1\zeta} = 0.0317\,\text{rad}^{-1}$, $C_{n\zeta} = -0.113\,\text{rad}^{-1}$, and $C_{y\zeta} = 0.160\,\text{rad}^{-1}$, respectively. From the plot of rolling moment coefficient, the results also show a significant dependence on angle of attack, with the aerodynamic performance of the rudder clearly superior at producing rolling moment for $\alpha < 0$ deg, than for $\alpha > 0$ deg. This result is clearly due to the reduced rudder effectiveness as the wing wake becomes more pronounced [29] at $\alpha > 0$ deg. This reduction is not seen for the results of change in yawing moment coefficient shown in the same figure, most probably due to the two results differing by an order of magnitude.

Comparing Figs. 10 and 11, it is clear that over the entire angle of attack range, the aerodynamic loading condition at $\beta = 10$ deg, significantly inhibits the performance of the rudder at achieving demanded deflection. From Fig. 11, with rudder input demanded to the windward side of the model, the favored final position of the rudder is between the freestream velocity vector and the body axis of the model. For demanded inputs to the leeward side, rudder performance improves significantly because now the aerodynamic load is assisting the positioning of the rudder. These results clearly indicate that sufficiently stiff control surface support systems, as well as accurate determination of the control surface position, are two priorities when using actively controlled models for estimating stability derivatives.

B. Evaluation of Dynamic Stability

Examples of the capabilities of the dynamic setup for measuring model responses to control surface excitation are shown in Figs. 12 and 13. From Fig. 12, the response of the model to a 0.5 Hz, 4 deg sine

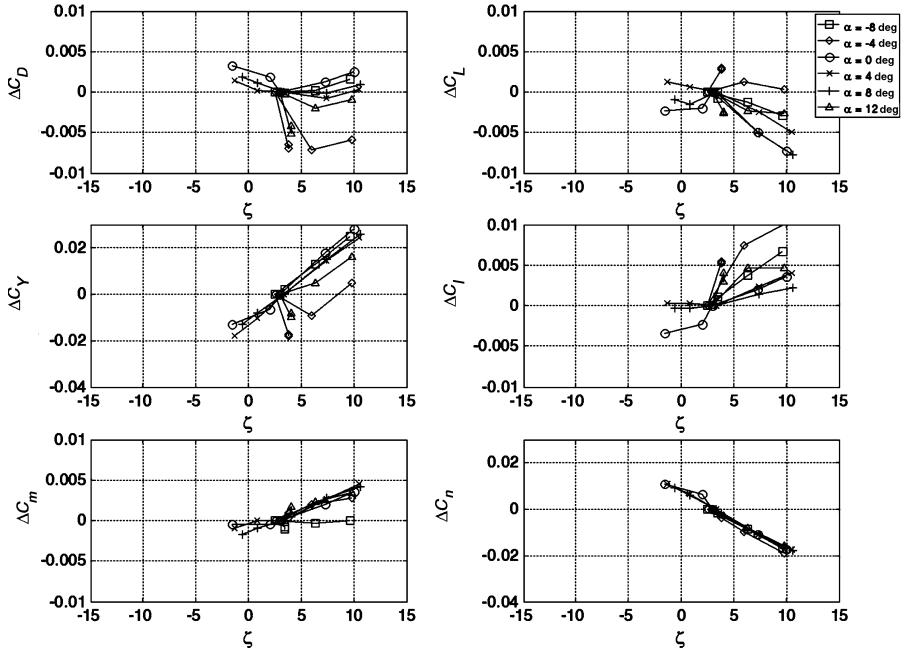

Fig. 11 Rudder effectiveness as a function of rudder deflection, $\beta = 10\,\mathrm{deg}$.

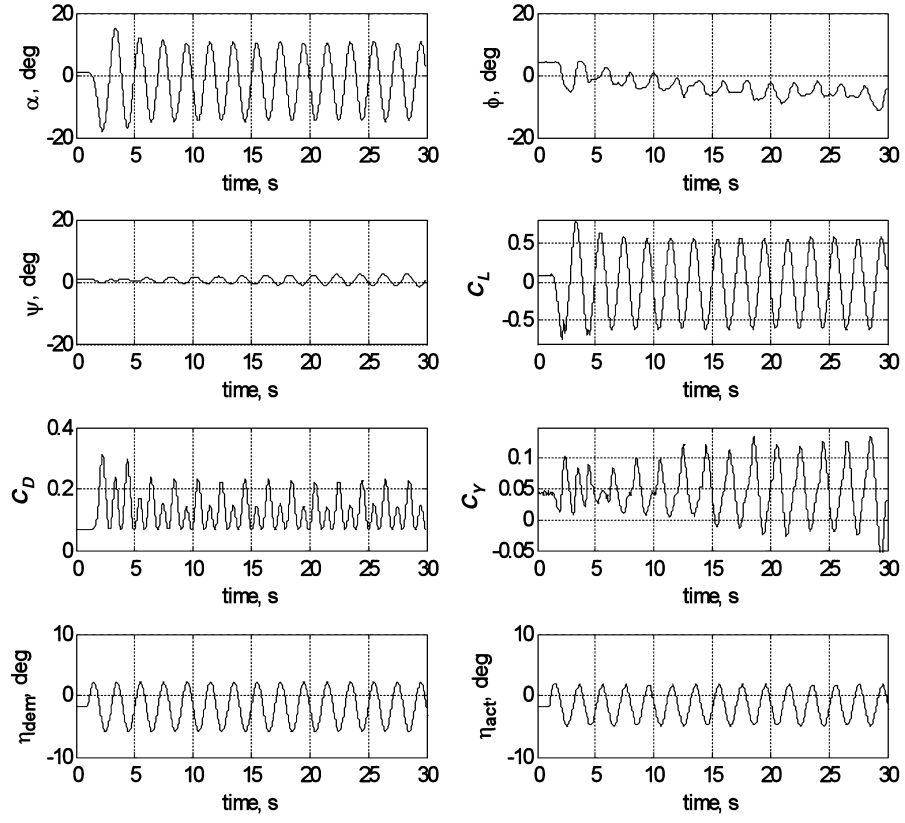

Fig. 12 Example of 3-DOF motion to forced oscillation input.

wave input shows significant deflections in all of the six degrees of freedom measured. On closer inspection, the lift and drag coefficients, together with the angle of attack time histories, show a pronounced change in magnitude as stabilator deflection changes. This is shown most vividly as an initial, transient overshoot, above the steady-state amplitude $t > 10$ s by as much as 30%–35%. Similar results were obtained in [30], with the delay in vortex breakdown suspected as the most likely cause. The response of the side force coefficient, roll, and yaw attitudes was much more subtle. For these three degrees of freedom, Fig. 12 indicates significantly smaller coupled deviations which, for this particular instance, are slowly diverging over time. This divergent behavior was uncharacteristic for most of the forced oscillation tests performed with most model responses reaching a stable, sustained oscillation, for the duration of the test period.

The response obtained for the drag coefficient shows a particularly interesting phenomenon. The frequency of oscillation is seen to double, whereas in actuality, it is the representation of the increase in drag as the model moves through both positive and negative angles of attack. The magnitude of each successive negative angle of attack

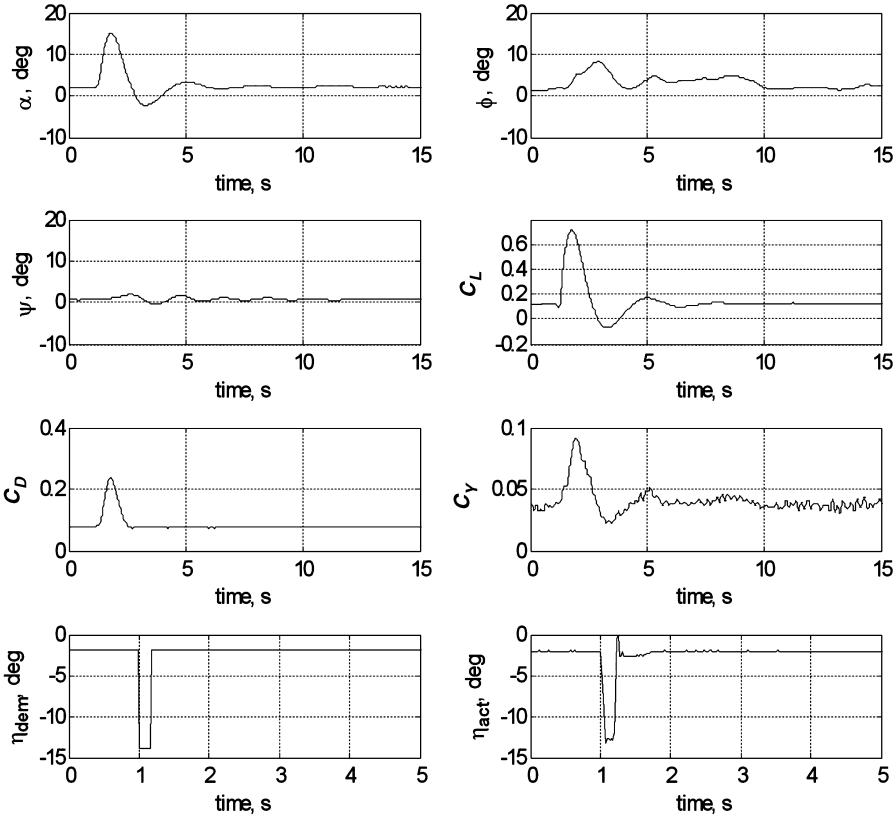

Fig. 13 Example of 3-DOF motion to impulse input.

peak is clearly more severe than the corresponding positive peak due to the mean angle of attack, for this oscillation case, being slightly negative. Further to this result, the initial value of drag coefficient, before excitation, was found to be significantly higher at $C_D = 0.066$ from that observed from static tests ($C_D \approx 0.026$) at the same angle of attack. This was possibly due to the need, between the static and dynamic phases of testing, to increase the size of the hole surrounding the 3-DOF gimbal to allow greater freedom of movement.

Figure 13 shows an example of the response of the model to stabilator impulse excitation. Similar to the forced oscillation results presented in Fig. 12, the model angle of attack, lift and drag coefficients show the most significant deviations, with all six degrees of freedom returning to initial conditions after excitation (see also Fig. 14). From the lift coefficient time history ($t \approx 1.2$ s), a small reduction in lift due to the deflection of the stabilator can be seen. This occurs before the large, subsequent increase in lift as the model rotates to large angles of attack [16]. This is also shown in Fig. 14 (pitch case) at the time increments of $t = 0.16$ s for the initial stabilator deflection, and at $t = 0.64$ s for the subsequent rotation of the model.

Unlike Fig. 12, the time history for drag coefficient presented in Fig. 13 was found to produce only one dominant peak. This was due to the model, under these test conditions, attaining insufficient rotation into the negative angle of attack range for the subsequent increase in drag to be detected. Evidence of this is also shown in Fig. 14. From the remaining plots in Fig. 13, all show similar trends and phase similitude with results obtained for the lift and drag coefficients but at significantly reduced magnitude. Additionally, from the time history of yaw attitude, it is also clear that the damping for this degree of freedom is appreciably less than that observed for pitch.

1. *State-Space Formulations*

A state-space representation for the short period, decoupled equations of motion, used for the reduction of all derivatives is presented in Eqs. (2–4). These equations assume linear and quasi-steady flow conditions [16,17]. To reduce the derivatives, a maximum likelihood/prediction error method estimation routine, generic to the Matlab system identification toolbox, was used. Using a "black-box" state-space modular structure, all of the concise derivatives were given freely adjustable assignments, with convergence achieved though minimizing the difference between experimentally measured and computed model responses. All derivatives were thereafter nondimensionalised [31].

$$\begin{bmatrix} \dot{u} \\ \dot{w} \\ \dot{q} \\ \dot{\alpha} \end{bmatrix} = \begin{bmatrix} x_q + x_{\dot{\alpha}} & x_\alpha \\ z_q + z_{\dot{\alpha}} & z_\alpha \\ m_q + m_{\dot{\alpha}} & m_\alpha \\ 1 & 0 \end{bmatrix} \cdot \begin{bmatrix} q \\ \alpha \end{bmatrix} + \begin{bmatrix} x_\eta \\ z_\eta \\ m_\eta \\ 0 \end{bmatrix} .\eta \tag{2}$$

$$\begin{bmatrix} \dot{v} \\ \dot{p} \\ \dot{r} \\ \dot{\phi} \end{bmatrix} = \begin{bmatrix} y_p & y_\phi \\ l_p & l_\phi \\ n_p & n_\phi \\ 1 & 0 \end{bmatrix} \cdot \begin{bmatrix} p \\ \phi \end{bmatrix} + \begin{bmatrix} y_\xi \\ l_\xi \\ n_\xi \\ 0 \end{bmatrix} .\xi \tag{3}$$

$$\begin{bmatrix} \dot{v} \\ \dot{p} \\ \dot{r} \\ \dot{\psi} \end{bmatrix} = \begin{bmatrix} y_r + y_{\dot{\psi}} & y_\psi \\ l_r + l_{\dot{\psi}} & l_\psi \\ n_r + n_{\dot{\psi}} & n_\psi \\ 1 & 0 \end{bmatrix} \cdot \begin{bmatrix} r \\ \psi \end{bmatrix} + \begin{bmatrix} y_\zeta \\ l_\zeta \\ n_\zeta \\ 0 \end{bmatrix} .\zeta \tag{4}$$

2. *Longitudinal Dynamic Derivatives*

Figures 15 and 16 show the results obtained for the forced and transient longitudinal stability derivatives, respectively. Where applicable, the variances from multiple repeated experiments, conducted under the same initial conditions, are included to gauge repeatability. From Fig. 15, the majority of derivatives were found to vary considerably with increasing reduced frequency, predominantly for the aerodynamic force and control derivatives. This behavior can be typical of ventrally mounted support systems and originates via convective lag [25,26,32–35] and cavity effects.

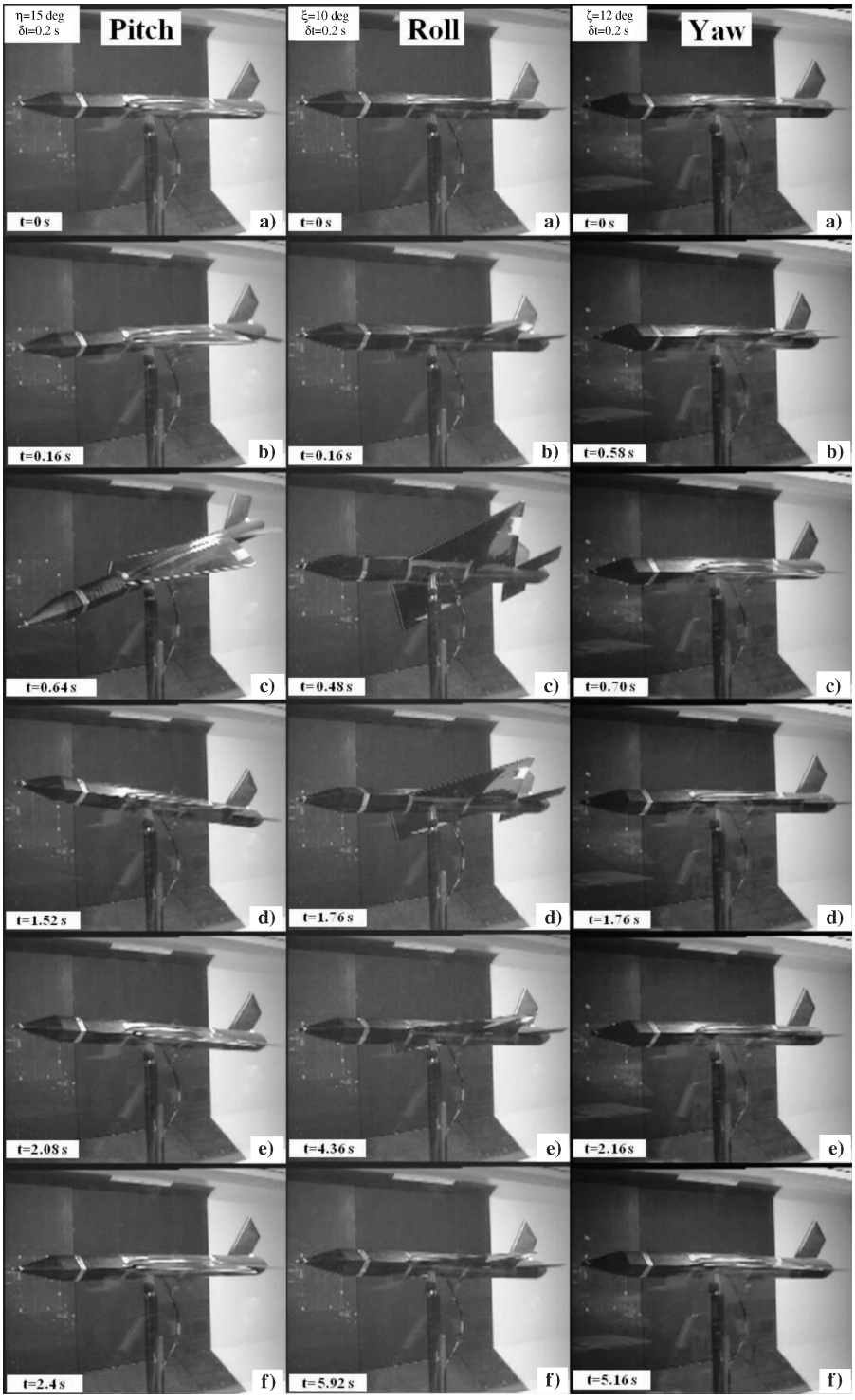

Fig. 14 Free pitch, roll, and yaw motions from control surface impulse excitation.

Additionally, as the reduced frequency increases, the achieved extremities of angle of attack of the model, for the same oscillation amplitude, are significantly reduced as can be seen in Table A4. This can reduce the influence of these effects on the results [32–35], allowing the more consistent trends and better agreement shown with the static and QinetiQ data. Comparing the values of $C_{m\alpha}$, $C_{m\eta}$, $C_{z\eta}$, and $C_{z\alpha}$ at high forcing frequencies to the static and QinetiQ data presented in Sec. III.A, all show reasonable to good agreement. Agreement between the results for the stiffness derivatives for the transient excitation case, presented in Fig. 16, is also very good, even though results for $C_{m\alpha}$ and $C_{z\alpha}$ seem to be somewhat underestimated. Also from Fig. 16, results for the stiffness and control derivatives in the streamwise direction show a clear linear trend with impulse excitation amplitude.

Results for the damping derivatives presented in Figs. 15 and 16 also show good agreement to the static and QinetiQ data. For the forced oscillation damping derivatives presented in Fig. 15, there is again a clear indication of the convective time lag effects evident in the control and stiffness derivatives discussed earlier. Figure 16, however, shows a different behavior. In this figure, the force damping derivatives show some degree of linearity with increase in stabilator deflection, although results obtained for the vertical force damping derivative, at positive stabilator deflections, are seen to be much more constant. For the pitching moment damping derivative,

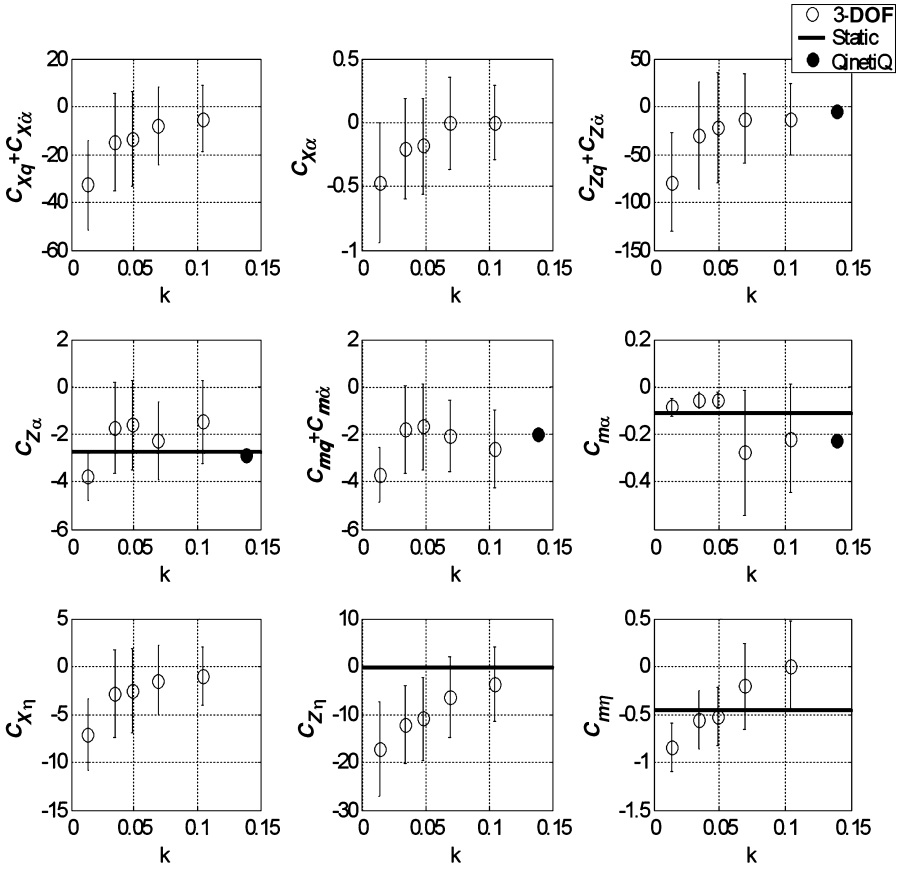

Fig. 15 Forced oscillation longitudinal stability derivatives.

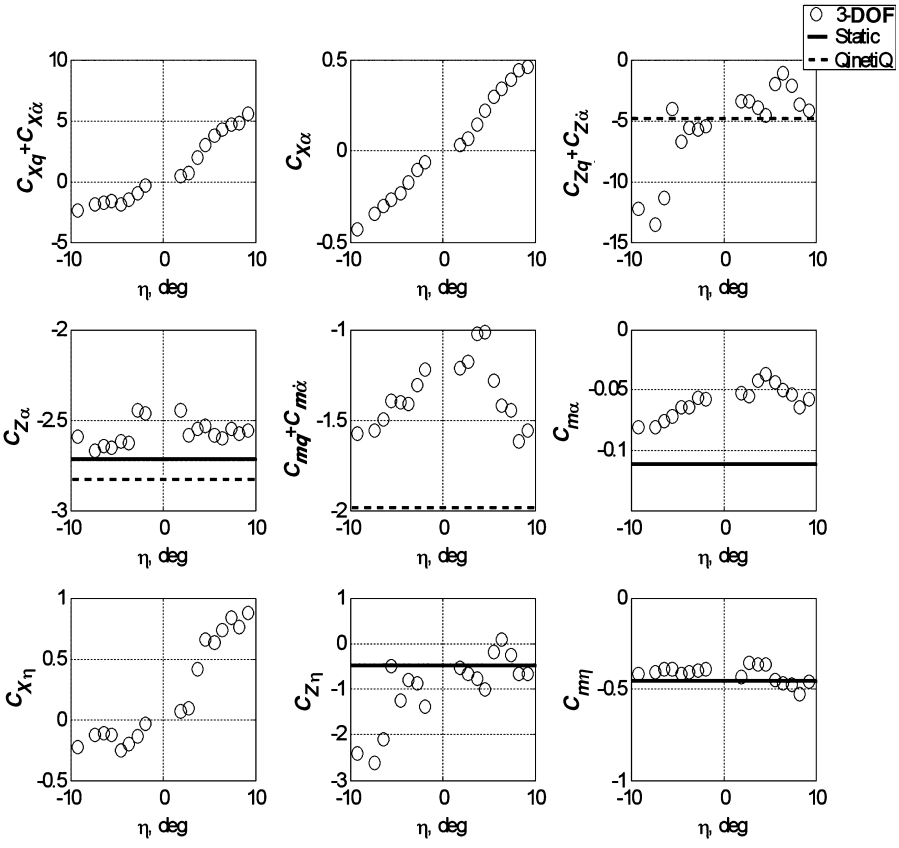

Fig. 16 Transient longitudinal stability derivatives.

results also show that at large impulse excitations, the damping characteristics of the model are as much as 40%–50% more than results obtained at smaller excitation amplitudes. This behavior was found to be symmetric about $\eta = 0$ deg.

To gauge the effectiveness of the parameter estimation routine, an example of the fit achieved between the experimentally obtained and computed response data is presented in Fig. 17. From the four variables used from Eq. (2), the plots of change in pitch rate, change in angle of attack, and vertical acceleration, all show excellent agreement. This performance was typical of the routine for the majority of test cases analyzed. For the plot of horizontal acceleration, however, only general agreement was found with the

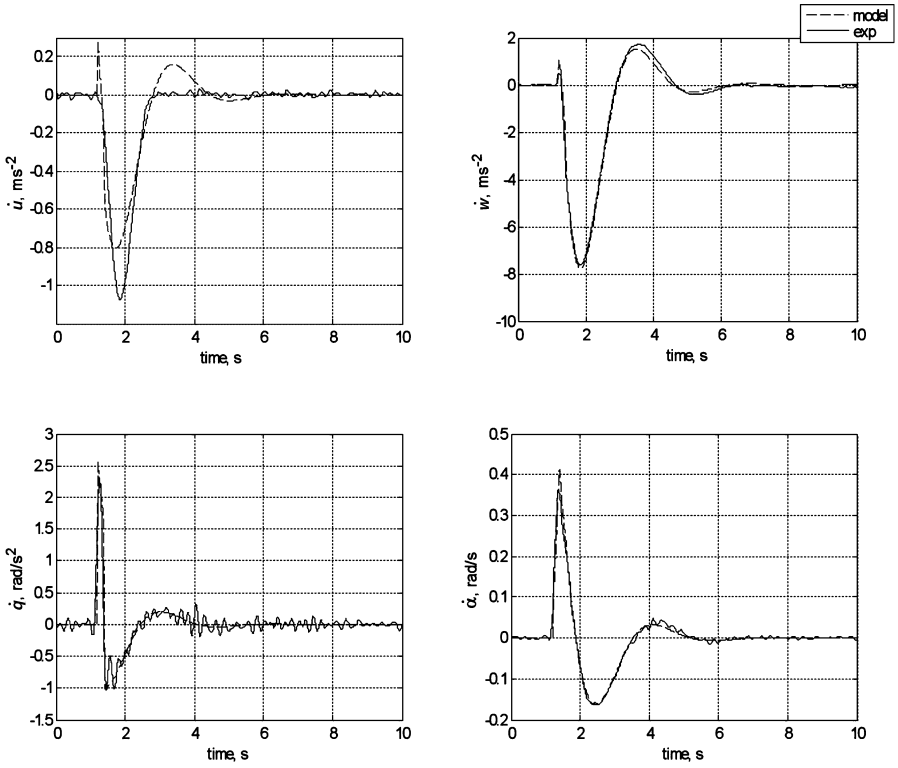

Fig. 17 Example of fit between modeled and experimental data for longitudinal derivatives.

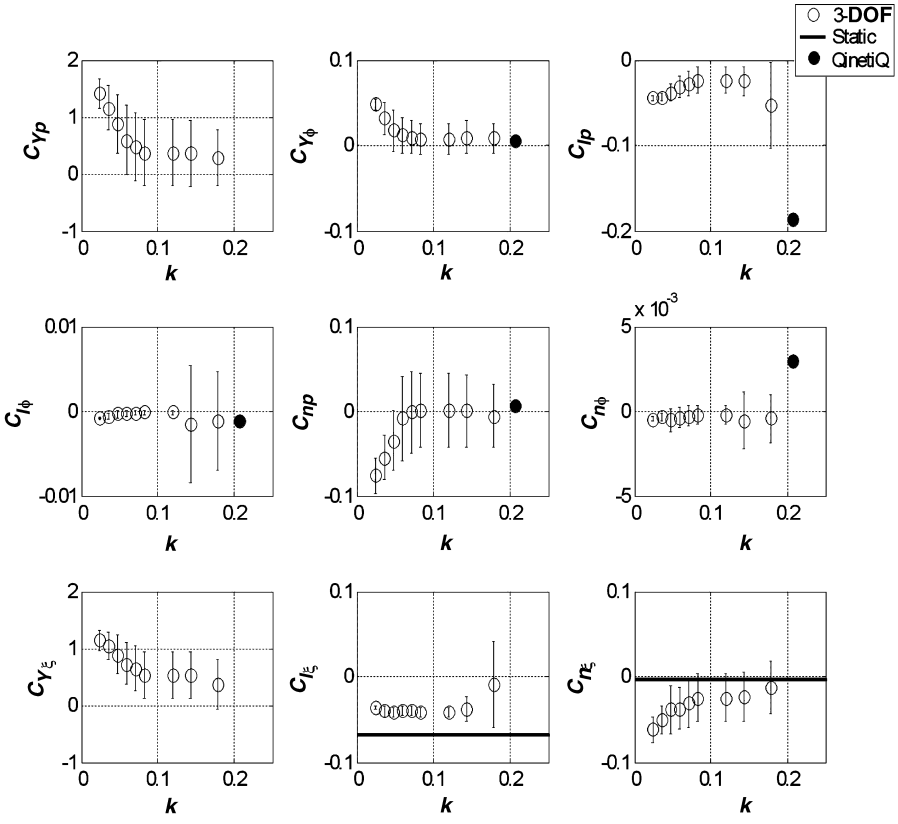

Fig. 18 Forced oscillation roll stability derivatives.

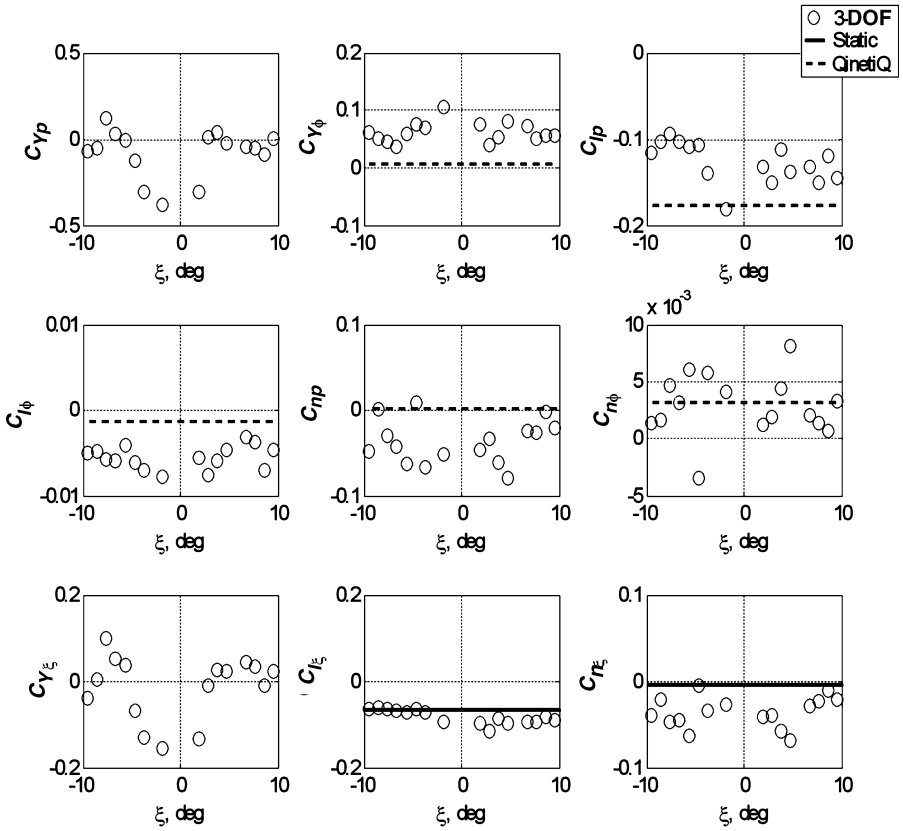

Fig. 19 Transient roll stability derivatives.

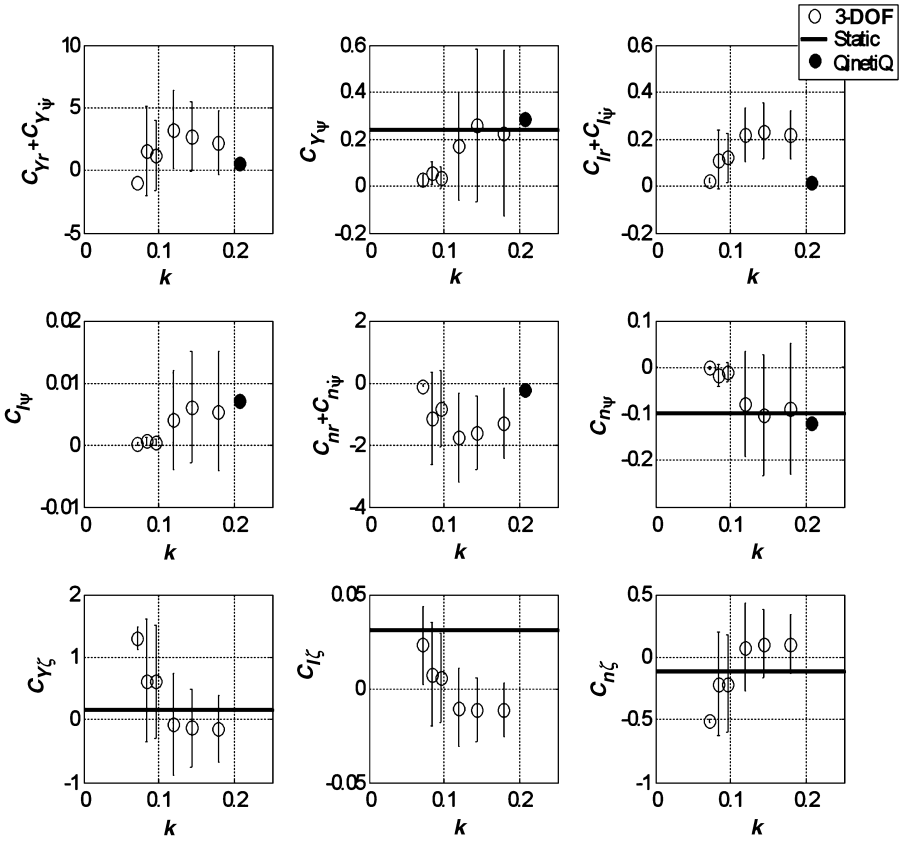

Fig. 20 Forced oscillation yaw stability derivatives.

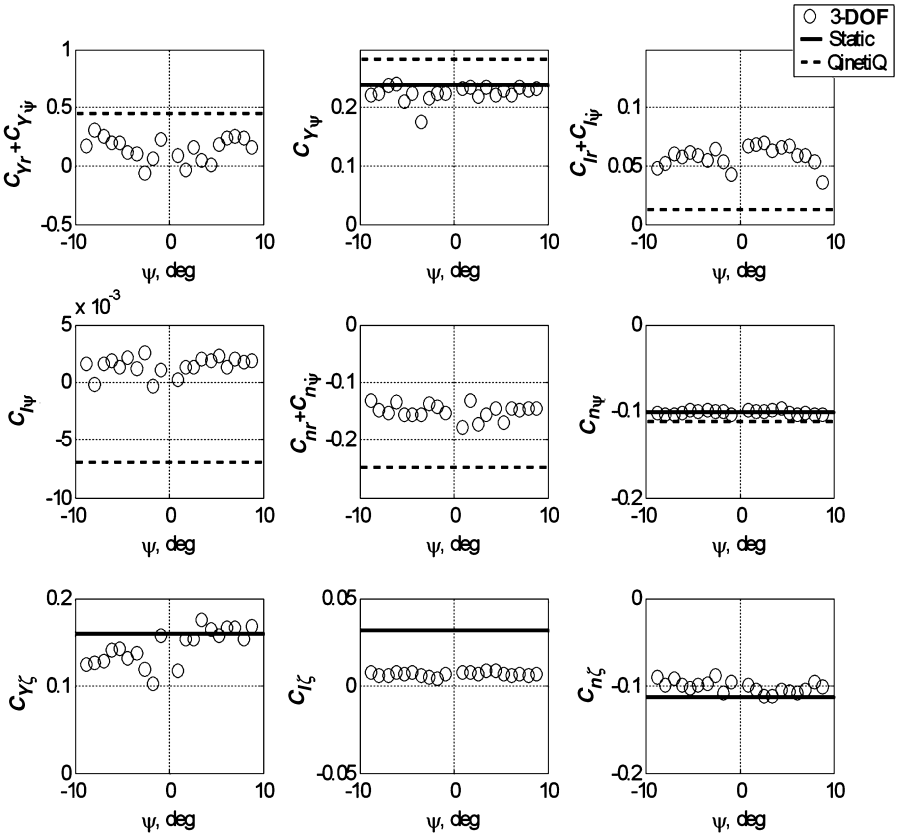

Fig. 21 Transient yaw stability derivatives.

predicted results. For this variable, the routine underestimated the maximum amplitude together with overestimating the subsequent peaks ($t > 3$ s) and initial influence of control surface deflection ($t \approx 1$ s).

3. Lateral Dynamic Derivatives

Figures 18–21 show the results obtained from the parameter estimation routine for the roll and yaw degrees of freedom. For the forced roll mode shown in Fig. 18, the majority of stability derivatives show similar variations with reduced frequency as that already discussed in reference to Fig. 15. For $k > 0.1$, results are clearly more consistent and in better agreement to both the static and QinetiQ forced data than those found at $k < 0.1$. Considering both Fig. 18 and 19, results for all stiffness and control derivatives were found to compare reasonably well to both the static and QinetiQ data, with the rolling moment control derivative in Fig. 19 being particularly good. As would be expected, the side force control derivative shows symmetry about $\xi = 0$ deg, indicating that deflection of the ailerons produces a subtle amount of side force, the degree of which is clearly more significant at lower aileron deflections ($C_{Y\xi} \approx -0.2@\xi = 2$–$4$ deg) than at $\xi = \pm 10$ deg ($C_{Y\xi} \approx 0$). Additionally, comparing Figs. 18 and 19, both $C_{1\phi}$ and $C_{n\phi}$ are negligibly small indicating that the model has very little stiffness in roll as well as adverse yaw due to roll. This lack of yaw due to roll was also observed visually during the tests with an example included in Fig. 14 (roll case) for a qualitative comparison.

Results for the forced and transient damping derivatives shown in Figs. 18 and 19 also show good agreement to the static and forced QinetiQ data presented. The exception to this was the poor agreement observed in the comparison between results from the forced QinetiQ testing and those of the current study for roll damping. This was thought to be due to a combination of the effect of the large cavity and the convective aerodynamic lag [25,26,32–35]. For the roll damping derivative presented in Fig. 19, the agreement improved considerably and was most probably due to the transient nature of the motion.

Results presented in Figs. 20 and 21 for the yaw degree of freedom also indicate that roll due to yaw $C_{1\psi}$, like yaw due to roll presented in Figs. 18 and 19, was very small. Results for $C_{n\psi}$ and $C_{Y\psi}$ both show good agreement, particularly in Fig. 21, with results from the static tests and supplied forced oscillation data. Control derivatives from Fig. 20, particularly side force and yaw, were also found to produce good correlation with the static data presented in Sec. III.A. This agreement was predominantly at higher values of reduced frequency, although the agreement for the roll control derivative improved for lower reduced frequencies. Considering Fig. 21, all derivatives presented show very little variation with rudder deflection amplitude. This is unexpected due to the high levels of model yaw angle, particularly at high rudder deflections, achieved from the response motion.

Comparison of the supplied forced oscillation data to transient results indicates most of the damping derivatives, with the exception of roll damping due to yaw, gave contradictory performance. For the yaw and side force damping derivatives, estimates were overpredicted for the forced oscillation case ($k > 0.1$), but underpredicted for the transient excitation case. Roll damping due to yaw was overpredicted in both cases. For both excitation cases, however, the yaw damping derivative due to yaw clearly indicates the model to be dynamically stable, albeit, for the transient case, at a significantly reduced level.

IV. Conclusion

Attempts to investigate the use of a dynamically flying, fully active, wind tunnel model mounted on a purposely designed, three degree-of-freedom gimbal support connected to a dynamic force and moment balance, have shown an ability to provide overall aerodynamic and stability information in a relatively efficient and cost-effective manner. Using this configuration, and through executing only small changes in the overall setup depending on the need for static or dynamic data, a significant amount of information relating to the performance of the wind tunnel model was obtained. Comparisons of the data obtained in both static and dynamic phases of the testing, as well as that obtained from a second independent source, showed reasonable to good agreement.

Appendix: Summary of M2370 Data

Table A1 Static stability derivatives determined from static testing

Quantity	Value	Error (95% conf.), rad^{-1}
$C_{Y\beta}$	-0.238 rad^{-1}	± 0.161 rad^{-1}
$C_{1\beta}$	-0.094 rad^{-1}	± 0.032 rad^{-1}
$C_{n\beta}$	0.101 rad^{-1}	± 0.011 rad^{-1}
$C_{L\alpha}$	2.72 rad^{-1}	± 0.245 rad^{-1}
$C_{m\alpha}$	-0.112 rad^{-1}	± 0.016 rad^{-1}
C_{Do}	0.023	± 0.003
k	0.330	± 0.007
$K_{n(\mathrm{avg})}(-10 < \eta < 10)$	$0.061\bar{\bar{c}}$	$\pm 0.026\bar{\bar{c}}$
$C_{1\xi}$	-0.068 rad^{-1}	± 0.005 rad^{-1}
$C_{n\xi}$	-0.004 rad^{-1}	± 0.001 rad^{-1}
$C_{1\zeta}$	0.031 rad^{-1}	± 0.014 rad^{-1}
$C_{n\zeta}$	-0.113 rad^{-1}	± 0.019 rad^{-1}
$C_{Y\zeta}$	0.160 rad^{-1}	± 0.040 rad^{-1}
$C_{L\eta}$	0.491 rad^{-1}	± 0.028 rad^{-1}
$C_{m\eta}$	-0.454 rad^{-1}	± 0.022 rad^{-1}

Table A2 Model trim angle and static margin with stabilator deflection

η_{dem},deg	η_{act}, deg	Model trim AOA, deg	Uncertainty (95% conf.), deg	K_n% of $\bar{\bar{c}}$	95% conf. error % of $\bar{\bar{c}}$
-10	-8.4 ± 1.8	28.1	13.6–90.2	6.2	± 3.8
-5	-4.7 ± 1.2	7.2	1.6–23.4	6.6	± 3.1
0	-0.8 ± 1.0	-16.8	-15.1 to -20	5.5	± 1.6
5	3.4 ± 1.5	-31.3	-26.3 to -40.8	6.8	± 2.2
10	7.2 ± 2.1	-61.1	-46.5 to -94.9	5.6	± 2.3

Table A3 Control surface response to demanded input

Stabilators, η_{dem}, deg	η_{act}, deg	Error (95% conf.), deg
-10	-8.4	± 1.7
-5	-4.7	± 1.2
0	-0.8	± 1.1
5	3.4	± 1.5
10	7.2	± 2.1
Ailerons, ξ_{dem}, deg	ξ_{act}, deg	Error (95% conf.), deg
-10	-8.7	± 0.5
-5	-4.3	± 0.3
0	1.1	± 0.4
5	4.9	± 0.3
10	9.3	± 0.5

Rudder, ζ_{dem}, deg	ζ_{act}, deg		Error (95% conf.), deg	
	$\beta = 0$ deg	$\beta = 10$ deg	$\beta = 0$ deg	$\beta = 10$ deg
-10	-7.1	1.8	± 0.7	± 2.8
-5	-3.9	2.1	± 0.4	± 3.0
0	0.7	2.9	± 1.1	± 0.4
5	3.8	6.5	± 0.6	± 1.0
10	6.9	8.85	± 0.7	± 0.6

Table A4 Response of model to control surface deflection (selected cases)

	Pitch	
k	η, deg	α, deg
0.014	± 2.17	± 15.04
0.035	± 1.98	± 7.15
0.049	± 1.81	± 2.06
0.069	± 1.78	± 1.85
0.104	± 3.58	± 2.68
	Roll	
k	ξ, deg	ϕ, deg
0.024	± 1.26	± 25.87
0.059	± 1.83	± 12.46
0.084	± 1.81	± 11.56
0.119	± 1.82	± 8.41
0.179	± 4.67	± 7.74
	Yaw	
k	ζ, deg	ψ, deg
0.084	± 1.42	± 3.06
0.119	± 1.43	± 1.21
0.178	± 1.59	± 0.81

Acknowledgments

This work was carried out under the terms of Contract CU004-26949 for the Managing Director of Future Systems Technology, QinetiQ, Ltd., Cody Technology Park, Farnborough, Hants, GU14 OLX England, United Kingdom. Funding was provided through the United Kingdom Ministry of Defense under the Applied Research Program.

References

[1] Green, L. L., and Spence, A. M., "Applications of Computational Methods for Dynamic Stability and Control Derivatives," AIAA Paper 2004-0377, Jan. 2004.

[2] Saephan, S., Van Dam, C. P., Fremaux, C. M., and Dalbello, T., "Simulation of Flow about Rotating Forebodies at High Angles of Attack," *Journal of Aircraft*, Vol. 41, No. 6, 2004, pp. 1298–1305.

[3] Tristant, D., and Beyers, M., "Oscillatory Coning," Rotary-Balance Testing for Aircraft Dynamics, AGARD Rept. 265, Dec. 1990.

[4] Gili, P. A., and Battipede, M., "Experimental Validation of the Wing Dihedral Effect Using a Whirling Arm Equipment," *Journal of Aircraft*, Vol. 38, No. 6, 2001, pp. 1069–1075.

[5] Hahne, D. E., Wendel, T. R., and Boland, J. R., "Wind-Tunnel Free-Flight Investigation of a Supersonic Persistence Fighter," NASA TP-3258, Feb. 1993.

[6] Bennett, R., Farmer, M., Mohr, R., and Hall, W., "Wind-Tunnel Technique for Determining Stability Derivatives from Cable-Mounted Models," *Journal of Aircraft*, Vol. 15, No. 5, 1978, pp. 304–310.

[7] Magill, J. C., Cataldi, P., Morency, J. R., Hammer, D. X., and Anderson, B. D., "Design of a Wire Suspension System for Dynamic Testing in AEDC 16T," AIAA Paper 2003-0452, Jan. 2003.

[8] Cook, M. V., "On the use of Small Scale Aircraft Models for Dynamic Wind Tunnel Investigation of Stability and Control," *Transactions of the Institute of Measurement and Control*, Vol. 9, No. 4, 1987, pp. 190–197.

[9] Subke, H., "Test Installations to Investigate the Dynamic Behavior of Aircraft with Scaled Models in Wind Tunnels," *Transactions of the Institute of Measurement and Control*, Vol. 1, No. 3, 1979, pp. 135–140.

[10] Jordan, F. L., and Hahne, D. E., "Wind-Tunnel Static and Free-Flight Investigation of High-Angle-of-Attack Stability and Control Characteristics of a Model of the EA-6B Airplane," NASA TP-3194, May 1992.

[11] Taylor, G. S., Gursul, I., and Greenwell, D. I., "Investigation of Support Interference in High-Angle-of-Attack Testing," *Journal of Aircraft*, Vol. 40, No. 1, 2003, pp. 143–152.

[12] Young, J., and Lai, J. C. S., "Oscillation Frequency and Amplitude Effects on the Wake of a Plunging Airfoil," *AIAA Journal*, Vol. 42, No. 10, 2004, pp. 2042–2052.

[13] Ahn, S., Choi, K.-Y., and Simpson, R., "Design and Development of a Dynamic Pitch-Plunge Model Mount," AIAA Paper 89-0048, Jan. 1989.

[14] Owens, D. B., Capone, F. J., Hall, R. M., Brandon, J. M., and Chambers, J. R., "Transonic Free-to-Roll Analysis of Abrupt Wing Stall on Military Aircraft," *Journal of Aircraft*, Vol. 41, No. 3, 2004, pp. 474–484.

[15] Capone, F. J., Owens, D. B., and Hall, R. M., "Development of a Transonic Free-to-Roll Test Capability," *Journal of Aircraft*, Vol. 41, No. 3, 2004, pp. 456–463.

[16] Rajamurthy, M., "Generation of Comprehensive Longitudinal Aerodynamic Data Using Dynamic Wind-Tunnel Simulation," *Journal of Aircraft*, Vol. 34, No. 1, 1997, pp. 29–33.

[17] Balakrishna, S., Niranjana, T., Rajamurthy, M. S., Srinathkumar, S., Rajan, S. R., and Singh, S. K., "Estimation of Aerodynamic Derivatives Using Dynamic Wind Tunnel Simulation Technique," Deutschen Zentrums für Luft- und Raumfahrt, Mitteilung 93-14, Brunswick, Germany, Dec. 1993, pp. 289–298.

[18] Kyle, H., "An Investigation into the use of a Pendulum Support Rig for Aerodynamic Modeling," Ph.D. Dissertation, Dept. of Aerospace Engineering, Univ. of Bristol, Bristol, UK, 2004.

[19] Magill, J., Darden, L., and Komerath, N., "Flow Visualization during Multiple-Axis Motions Using a Wind-Driven Manipulator," *Journal of Aircraft*, Vol. 33, No. 1, 1996, pp. 163–170.

[20] Pedreiro, D., "Development of an Apparatus for Wind Tunnel Dynamic Experiments at High Alpha," NASA CR-203713, Feb. 1997.

[21] Cook, N. J., "A Sensitive 6-component High-Frequency-Range Balance for Building Aerodynamics," *Journal of Physics E: Scientific Instruments*, Vol. 16, No. 5, 1983, pp. 390–393.

[22] O'Leary, C. O., "Wind-Tunnel Measurement of Aerodynamic Derivatives Using Flexible-Sting Rigs," Dynamic Stability Parameters, AGARD LS 114, March 1981.

[23] O'Leary, C. O., "Oscillatory Data for Typical Configurations," Special Course on Aircraft Dynamics at High Angles of Attack: Experiments and Modelling, AGARD Rept. 776, April 1991.

[24] O'Leary, C. O., "Relation Between Rotary and Oscillatory Test Results," Rotary-Balance Testing for Aircraft Dynamics, AGARD Rept. 265, Dec. 1990.

[25] Orlik-Ruckemann, K., "Aerodynamic Aspects of Aircraft Dynamics at High Angles of Attack," *Journal of Aircraft*, Vol. 20, No. 9, 1983, pp. 737–752.

[26] Johnson, J. L., Grafton, S. B., and Yip, L. P., "Exploratory Investigation of the Effects of Vortex Bursting on the High Angle-Of-Attack Lateral-Directional Stability Characteristics of Highly-Swept Wings," AIAA Paper 80-0463, March 1980.

[27] Skow, A. M., and Titiriga, A., "A Survey of Analytical and Experimental Techniques to Predict Aircraft Dynamic Characteristics at High Angles of Attack," Dynamic Stability Parameters, CP-235AGARD, Neuille Sur Seine, France, Nov. 1978, Paper 19.

[28] Taylor, G. S., and Gursul, I., "Buffeting Flows over a Low-Sweep Delta Wing," *AIAA Journal*, Vol. 42, No. 9, 2004, pp. 1737–1745.

[29] Hebbar, S. K., and Leedy, D. H., "A Laser Sheet Flow Visualization and Aerodynamic Force Data Evaluation of a 3% YF-17 Fighter Aircraft Model at High Angles of Attack," AIAA Paper 90-3019, Aug. 1990.

[30] Thompson, S., Batill, S., and Nelson, R., "Unsteady Surface Pressure Distributions on a Delta Wing Undergoing Large Amplitude Pitching Motions," AlAA Paper 90-0311, Jan. 1990.

[31] Cook, M. V., *Flight Dynamics Principles*, Wiley, New York, 1997, pp. 113–176.

[32] Beyers, M. E., and Ericsson, L. E., "Ground Facility Interference on Aircraft Configurations with Separated Flow," *Journal of Aircraft*, Vol. 30, No. 5, 1993, pp. 682–688.

[33] Ericsson, L. E., and Reding, J. P., "Dynamic Support Interference in High Alpha Testing," AIAA Paper 1986-760, March 1986.

[34] Reding, J. P., and Ericsson, L. E., "Dynamic Support Interference," *Journal of Spacecraft and Rockets*, Vol. 9, No. 7, 1972, pp. 547–553.

[35] Ericsson, L. E., "Another Look at High-Alpha Support Interference in Rotary Tests," *Journal of Aircraft*, Vol. 28, No. 9, 1991, pp. 584–591.